Simulating the molecular density distribution during multi-phase fluid intrusion in heterogeneous media

Mingzhi Wang[a,b,c*,#], Beimeng Qi[d,#], Yushi Liu[a,b,c], Abir Al-Tabbaa[e], Wei Wang[a,b,c]

[a#] School of Civil Engineering, Harbin Institute of Technology, Harbin, 150090, CN

[b] Key Lab of Structures Dynamic Behavior and Control of the Ministry of Education, Harbin Institute of Technology, Harbin, 150090, CN

[c] Key Lab of Smart Prevention and Mitigation of Civil Engineering Disasters of the Ministry of Industry and Information Technology, Harbin Institute of Technology, Harbin, 150090, CN

[d#] College of Quality & Safety Engineering, China Jiliang University, Hangzhou, 310018, CN

[e] Department of Engineering, University of Cambridge, Cambridge, CB2 1PZ, UK

*Corresponding author.

E-mail address: mwang@hit.edu.cn (M. Wang);

[#]These authors and affiliations contributed equally to this work.

Abstract

A computational recovery of multi-phase intrusion was discussed with the modified multi-relaxation time Lattice Boltzmann method (MRT-LBM). Originally proposed dual-matrix computation is developed to address the different phase separation and interface tracking for the multi-phase problem. A comprehensive validation is performed with the previously theorized observation of the mercury-water system. Results show that the dual-matrix computation is feasible to provide converged output under narrowed density difference down to 18%. The wetting and non-wetting behaviour resulted from form solid-fluid interaction is realized with arbitrary boundaries, in which the contact variance

is up to 4.14%. The linear relations described by Laplace's law and Washburn's equation were three-dimensionally recovered with determination coefficients of 96.34% and 94.19%, respectively. A third fluid intrusion status of partial-intrusion is captured in addition to complete-intrusion and non-occupation in porous boundary, demonstrating the advanced function of the phase-separation and interface tracking in problems with further increased heterogeneity.

Keywords: Porous media; Multi-phase fluid; Surface tension; Molecular density distribution; Lattice Boltzmann method

1. Introduction

Multi-phase fluid intrusion into porous networks is a phenomenon commonly existing in problems of lipid transportation (Lacatusu et al., 2019), petroleum extraction (Negahban et al., 2020), organic matter emulsions (Perazzo et al., 2015) and carbon sequestration (Espinet and Shoemaker, 2013). Intrusive fluid plays a crucial part in the above natural and engineering processes, where a fluid phase pushes through a solid medium immersed in another liquid phase (Huppert, 1986). A comprehensive understanding of the behaviour directs the design and engineering of fluid network and porous media. Experimentally, the intrusion behaviour was studied with homogeneous properties such as pressure, turbulence intensity and flow rate (Coasne et al., 2009; Wang et al., 2018). Although experimental observation contributed to a macroscopic understanding of the multi-phase fluid behaviour, it was pointed out that the microscopic interphase detection was inadequate with common approaches (Hudgins, 1981). More specifically, porous media's opacity raises the difficulty to capture the molecular density distribution within (Thomas et al., 2004). Hence, the essential information of 3-dimensional molecular density distribution is in absence.

Alternatively, computational fluid dynamics (CFD) suggests a computational realization to simulate the intrusive problem (Thabet and Thabit, 2018). Macroscopically, Navier-Stokes (NS) equations following incompressible assumption offer a solution for intrusion behaviour in relatively large water bodies (Cantero et al., 2007; Ungarish, 2005). Microscopically, molecular dynamics (MD) following the spherical assumption have been adopted to simulate intrusion in nanoscale and below (Coasne et al., 2009; Kim et al., 2019). Lattice Boltzmann method (LBM) is a mesoscale methodology simultaneously considering the local molecular density and global fluid behaviour (Zhang, 2014), where both the incompressible assumption and spherical assumption are invalid (Raabe, 2004). In practice, modelling water transport in systems such as soil particles (Sun, 2018), cement particles (Zhou et al., 2017), and blood vessels (Tiwari and Chauhan, 2019) requires mesoscale methodology because of the intermediate Knudsen number (Pourfattah et al., 2020). More specifically, the above micrometre media's characteristic system length is not large enough to neglect the discontinuity in the fluid-surface region in NS solution (Basser et al., 2017). The MD solution focusing on molecules and atoms in media in μm^3 requires particles amount to a magnitude order of 10^{16}, overwhelming the affordable budget (Lane et al., 2010). Additionally, a mathematical description alternative to analytical geometry must process the heterogeneous boundary of arbitrary media. In previous porous formation studies, voxel-based algorithms were developed to realize random media processing (Byholm et al., 2009; Tian et al., 2020; Wang et al., 2019). To sum, the 3D matrix-based LBM for intermediate Knudsen number (Raabe, 2004) is a feasible CFD solver with adaptability to computational chemistry to provide 3D molecular density distribution in heterogeneous media.

The intrusion phenomenon study was initiated form the capillary fluid dynamics proposed by Washburn equations (Edward W. Washburn, 1921). The classic model adopted parallel tubes as the solid boundary for mercury intrusion (E. W. Washburn, 1921). Governing by the surface tension described by Laplace's law, the local difference in capillary interconnection was reflected by the various access of the intruding fluid under the same pressure (Valentinuzzi et al., 2011). Modern fluid dynamics has been developed into two directions, which are top-down and bottom-up approaches (Seiffert, 2017). The top-down philosophy on intrusion simulation was demonstrated by the attempts to solve the partial differential equations integrating NS equations, Washburn equations and Laplace equations (Limache et al., 2007; Tarek and Lee, 2018). On the other hand, the bottom-up approaches such as MD and LBM assembled the small scale mechanism to recover from large scale phenomenon (Yoshimoto et al., 2013). Classic models function as endpoint validation instead of the starting point calculation in the latter approach. MD recovery of the surface tension emphasized the Newtonian interaction among molecules and atoms (Yoshimoto et al., 2013), in which the microscale intrusion simulation results were compared with the Laplace equation (Park et al., 2001) and Washburn equation (Dimitrov et al., 2007). However, the abovementioned problem of the computational budget forced MD solutions to adopt simplified boundary of free volume (Park et al., 2001) and single tube (Coasne et al., 2009; Dimitrov et al., 2007; Kim et al., 2019), preventing further extension in arbitrary media. LBM recovery of the multi-phase phenomenon emphasizes the statistical distribution of local fluid density with the Boltzmann equation (Zhang and Tian, 2008). Previous 2D LBM attempts (Baakeem et al., 2020; Hyväluoma et al., 2004) on the mesoscale intrusion demonstrated the feasibility of recovering surface tension with the Shan-Chen model (Shan and Chen, 1994). To further develop the LBM methodology for intrusion problem, the following aspects should be contributed. Firstly, the single relaxation time (SRT) collision operator (Bhatnagar et al., 1954; Qian et al., 1992) adopted in previous solutions can be upgraded with the latest multi relaxation time (MRT) collision operator to improve the computational stability (Coreixas et al., 2020). The streaming calculation with a single matrix should be modified to provide confirmative phase separation (Lee et al., 1998) and straightforward data registration (Khare et al., 2019) during the multi-phase interface detection. More importantly, a 3D realization is needed to prepare the method for realistic problems.

This paper proposed a 3D MRT-LBM scheme to simulate the mesoscale intrusion into arbitrary porous media. Mercury and water were adopted as comparing phases to dock the previous theory on capillary fluid dynamics. The scheme integrates the Shan-Chen model to compute the multi-phase redistribution through the bottom-up approach from surface tension recovery to macroscopic fluid behaviour. Validation with the Laplace equation and Washburn equations was performed in the previously reported cylindrical boundaries. The adaptability to arbitrary media was demonstrated by direct application in boundary-free volume, solid surface, single tube, parallel tubes and random porous media. The dual-matrix computation enables the registration of the multi-phase fluid for in-process monitoring. The work demonstrates an LBM solution to simulate molecular density distribution during the intrusion into heterogeneous media.

2. Methods

2.1. Multi-relaxation time Lattice Boltzmann method (MRT-LBM)

The LBM engine in this study adopted D3Q19 MRT-LBM through independent programming (Wang, 2017). The core equations of the fluid density development were given by Eq. 1 (D'Humières et al., 2002) and Eq. 2 (Raabe, 2004).

$$\mathrm{f}(\mathbf{x}+\mathrm{e_i}\delta\mathrm{t}, \mathrm{t}+\delta\mathrm{t}) - \mathrm{f}(\mathbf{x}, \mathrm{t}) = -\mathrm{M}^{-1} \cdot S \cdot [\mathrm{M} \cdot \mathrm{f}(\mathbf{x}, \mathrm{t}) - \mathrm{M} \cdot \mathrm{f}^{eq}(\mathbf{x}, \mathrm{t})] \quad (1)$$

$$\mathrm{f^{eq}}(\mathbf{x}, \mathrm{t}) = \mathrm{w_i}\rho[1 + \frac{\mathrm{e_i}\cdot\mathbf{u}}{\mathrm{c_s^2}} + \frac{(\mathrm{e_i}\cdot\mathbf{u})^2}{2\mathrm{c_s^4}} - \frac{\mathrm{e_i}\cdot\mathbf{u}}{2\mathrm{c_s^2}}] \quad (2)$$

Where $\mathrm{f}(\mathbf{x}, \mathrm{t})$ is the fluid density distribution, **x** is the lattice coordinates, t is the fluid progression time, M is the 19×19 transform matrix for MRT simulation (Premnath and Abraham, 2007) as given by **Appendix A**, S is the collision matrix for MRT simulation as provided by Eq. 3 (Premnath and Abraham, 2007), $\mathrm{f^{eq}}(\mathbf{x}, \mathrm{t})$ is the equilibrium density calculated with Maxwell-Boltzmann equilibrium distribution (Abdoul-Carime et al., 2015; Qian et al., 1992), $\mathrm{e_i}$ is the velocity vectors as given by Eq. 4 (Premnath and Abraham, 2007; Zhang et al., 2013), $\mathrm{w_i}$ is the density weighting factors as provided by Eq. 5 (Premnath and Abraham, 2007; Zhang et al., 2013), ρ is the macroscopic density distribution, ${\mathrm{c_s}}^2 = 1/3$ is the lattice sound speed, **u** is the macroscopic velocity distribution, and i is an integer between 0 to 18 for the D3Q19 simulation.

$$\mathrm{S} = \mathrm{diag}[1, 1.19, 1.4, 1, 1.2, 1, 1.2, 1, 1.2, 1, 1, 1, 1, 1, 1, 1, 1.98, 1.98, 1.98] \quad (3)$$

$$e_i = \begin{bmatrix} 0 & 0 & 0 & 1 & -1 & 0 & 0 & 1 & 1 & -1 & -1 & 0 & 0 & 0 & 0 & 1 & -1 & 1 & -1 \\ 0 & 1 & -1 & 0 & 0 & 0 & 0 & 1 & -1 & 1 & -1 & 1 & -1 & 1 & -1 & 0 & 0 & 0 & 0 \\ 0 & 0 & 0 & 0 & 0 & 1 & -1 & 0 & 0 & 0 & 0 & 1 & 1 & -1 & -1 & 1 & 1 & -1 & -1 \end{bmatrix} \quad (4)$$

$$w_i = [\tfrac{1}{3}, \tfrac{1}{18}, \tfrac{1}{18}, \tfrac{1}{18}, \tfrac{1}{18}, \tfrac{1}{18}, \tfrac{1}{18}, \tfrac{1}{36}, \tfrac{1}{36}, \tfrac{1}{36}, \tfrac{1}{36}, \tfrac{1}{36}, \tfrac{1}{36}, \tfrac{1}{36}, \tfrac{1}{36}, \tfrac{1}{36}, \tfrac{1}{36}, \tfrac{1}{36}, \tfrac{1}{36}] \quad (5)$$

The macroscopic density distribution was calculated with Eq. 6 (Chen and Doolen, 1998).

$$\rho(\mathbf{x}, t) = \sum_{i=0}^{18} f(\mathbf{x}, t) \quad (6)$$

Where $\tau = 1$ is a relaxation time related to the kinematic viscosity and F is the force applied to the lattice's liquid. The dual-matrix computation was further proposed by dividing the fluid matrix into two matrices representing phase-I and phase-II, respectively. Eq. 7-9 presents the formula to calculate 3D dual-phase fluid motion.

$$f(\mathbf{x}, t) = f_I(\mathbf{x}, t) + f_{II}(\mathbf{x}, t) \quad (7)$$

$$f_{I||II}(\mathbf{x} + e_i\delta t, t + \delta t) - f_{I||II}(\mathbf{x}, t) = -M^{-1} \cdot S \cdot [M \cdot f_{I||II}(\mathbf{x}, t) - M \cdot f_{I||II}{}^{eq}(\mathbf{x}, t)] \quad (8)$$

$$f_{I||II}{}^{eq}(\mathbf{x}, t) = w_i \rho_{I||II}[1 + \frac{e_i \cdot \mathbf{u}_{I||II}}{c_s^2} + \frac{(e_i \cdot \mathbf{u}_{I||II})^2}{2c_s^4} - \frac{e_i \cdot \mathbf{u}_{I||II}}{2c_s^2}] \quad (9)$$

The macroscopic velocity distribution was calculated with Eq. 10 and 11 (Benzi et al., 2006; Shan and Chen, 1993; Zhang, 2013).

$$u_I(\mathbf{x}, t) = \frac{1}{\rho_I(\mathbf{x}, t)} \sum_{i=0}^{18} f_I(\mathbf{x}, t) \cdot e_i + \frac{\tau F_I(\mathbf{x}, t)}{\rho_I(\mathbf{x}, t)} \quad (10)$$

$$u_{II}(\mathbf{x}, t) = \frac{1}{\rho_{II}(\mathbf{x}, t)} \sum_{i=0}^{18} f_{II}(\mathbf{x}, t) \cdot e_i + \frac{\tau F_{II}(\mathbf{x}, t)}{\rho_{II}(\mathbf{x}, t)} \quad (11)$$

The interaction between the two phases was accounted for through the computation of the inter-force. If the force terms take the value of zero, the two phases' motion will independently follow the Maxwell-Boltzmann equilibrium distribution, and no phase separation will be formed. In the mercury intrusion phenomenon, the phase separation between phase-I and phase-II is essential to obtain the phase progression paths. Therefore, the force term calculated with the Shan-Chen model (Shan et al.,

1993) was further introduced.

2.2. Integrating the Shan-Chen model

The fluid phases of the triple-phase simulation were initially registered as phase-I and phase-II. The solid phase was registered as phase-S. The force term of phase-I was calculated with Eq. 12

$$F_I(x,t) = F_{I-I}(x,t) + F_{I-II}(x,t) + F_{I-S}(x,t) \tag{12}$$

Where $F_I(x,t)$ is the force applied on the phase-I in the lattice of x, F_{I-I} is the force from the phase-I in the lattice other than x, F_{I-II} is the force form the phase-II in the lattice other than x and F_{I-S} is the force form the solid phase when the lattice x in contact with the tangible interface. F_{I-I}, F_{I-II} and F_{I-S} were calculated with Eq. 13-15, respectively, based on the original Shan-Chen model (Parmigiani et al., 2016; Shan et al., 1993).

$$F_{I-I}(x,t) = -G_{I-I}\psi_I(x,t)\sum_{i=1}^{18} w_i\, \psi_I(x+e_i,t) \tag{13}$$

$$F_{I-II}(x,t) = -G_{I-II}\psi_I(x,t)\sum_{i=1}^{18} w_i\, \psi_{II}(x+e_i,t) \tag{14}$$

$$F_{I-S}(x,t) = -G_{I-S}\psi_I(x,t)\sum_{i=1}^{18} w_i\, \psi_S(x+e_i,t) \tag{15}$$

G is an interaction coefficient; ψ is the effective mass calculated with Eq. 16 (Shan et al., 1993; Shan and Chen, 1993). G<0 represents attractive inter forces and G>0 represents repulsive forces. The density of the solid phase was fixed as $\rho_S = 5.3$.

$$\Psi(x,t) = 1 - e^{-\rho(x,t)} \tag{16}$$

The computation of the force terms F_{II} followed the same approach, and the involved coefficients of interaction were G_{II-II}, G_{II-I} and G_{II-S}. Table 1 presents the interaction coefficient adopted in this study.

G_{I-I}	G_{I-II}	G_{I-S}
-0.05	2.5	-0.1

G_{II-II}	G_{II-I}	G_{II-S}
-0.8	2.5	0.1

Table 1: Coefficient of interaction in the triple-phase Shan-Chen model

In the original Shan-Chen model, the bulk fluid phase's internal pressure was calculated with Eq. 17 (Benzi et al., 2006; He et al., 1999; Qin et al., 2018).

$$P(x,t) = \rho(x,t)c_s^2 + \frac{1}{2}c_s^2 G\psi(x,t)^2 \quad (17)$$

Where the right-hand consists of the density term and the interaction term. In this study, the density terms were considered the sum of the two phases, and the interaction term was expanded with the I-I, II-II, I-II interaction. Eq. 18 presents the modified formula for bulk pressure computation.

$$P = (\rho_I + \rho_{II})c_s^2 + \frac{1}{2}c_s^2(G_{I-I}{\psi_I}^2 + G_{II-II}{\psi_{II}}^2 + G_{I-II}\psi_I\psi_{II}) \quad (18)$$

2.3. Boundary conditions

Multiple simulations were performed with boundary-free volume, solid surface, single tube, parallel tubes and random porous media. The standard Laplace-Young test (Kuzmin and Mohamad, 2010; Parmigiani et al., 2016) was conducted within a 50×50×50 cubic volume, and periodic boundary condition was adopted on the six surfaces of the cube. The bubble formation was performed under the α group and β group with different density distribution. Surface droplet simulation was completed within a 20×40×40 volume to determine the contact angle. The volume's bottom surface was defined as solid-phase with no-slip bounce back condition (D'Humières et al., 2002). Single tube simulation was performed in a 30×30×100 virtual device as presented in Fig. 1(a), and no-slip bounce back condition was adopted on the liquid-solid interface. Parallel tubes simulation was performed in a 40×90×80 virtual device as illustrated in Fig. 1(b), and no-slip bounce back condition was adopted on the liquid-solid interface. The last simulation of intrusion into porous media was performed with an extracted structure from polydisperse particle packing (Wang et al., 2019), as presented in Fig. 1(c), whose porosity was 36.09%. The overall volume of the porous medium was 50×50×70. No-slip bounce back condition was adopted on the liquid-solid interface, top surface and bottom surface. Periodic boundary condition was assumed on the rest four surfaces of the volume.

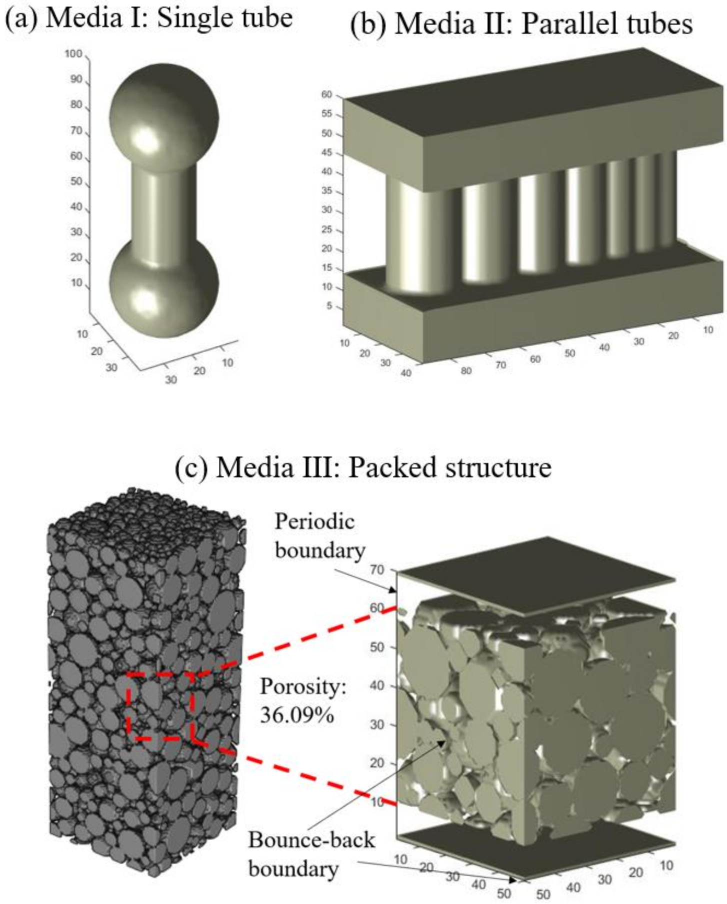

Fig. 1 (a) Previously reported boundary (Hou et al., 2019; Kim et al., 2019). (b) Classic multi-tube boundary. (c) The porous border in this work.

2.4. Molecular density

The density distribution $\rho(\mathbf{x}, t)$ of the LBM represents the number of molecules in 3D lattices (He and Luo, 1997). Table 2 presents the conversion from the molar volumes of water and mercury to the target LBM density. The target density was realized by the calibration of the interaction coefficients, including G_{I-I}, G_{I-II}, G_{II-S} G_{II-II}, G_{II-I} and G_{II-S}. The simulation was conducted until the steady-state was reached. In this study, the stable-state was defined as the iteration when the overall density change was within 0.5‰.

	Phase label	Phase-I	Phase-II

A	Chemical formula	H_2O	Hg
B	Mass density	10^3 kg/m^3	13.6×10^3 kg/m^3
C	Relative molecular mass	18	200
D	Mass of $\frac{\text{Carbon}-12}{12}$	1.66×10^{-27} kg	
E	Converted mass (C · D)	2.99×10^{-26} kg	3.32×10^{-25} kg
F	Avogadro constant	6.022×10^{23} mol^{-1}	
G	Molecule number density ($\frac{\text{B}}{\text{E}\cdot\text{F}}$)	5.56×10^4 mol/m^3	6.80×10^4 mol/m^3
H	Target LBM density (G_I: G_{II})	1	1.22

Table 2 Conversion from molecular properties to LBM density

3. Result and discussion

3.1. Laplace-Young test and fundamental performance

Fig. 2(a) presents the 3D visualized result of the bubble formation and the cross-sectional area for the 2D illustration. Fig. 2(b) shows the correlation between internal pressure difference and the radius of the bubble. The resulted pressure difference is inversely proportional to the radius of the bubble. The linear relationship of the Laplace testing equation, as given by Eq. 19, was recovered with a coefficient of determination of 96.34%.

$$P = \frac{\sigma}{R} \tag{19}$$

Where ΔP is the pressure difference between the internal region and the outer region of the bubble, σ is the surface tension term, and R is the radius of the bow. Previous Shan-Chen models also demonstrated Laplace's law's recovery with a single matrix computation (Shan and Chen, 1993). However, the origin point (0,0) was not always passed due to the multi-phase registration difficulty (Dauyeshova et al., 2018; Kuzmin and Mohamad, 2010; Qin et al., 2018). In this study, the proposed method makes the multi-phase registration, as presented in Fig. 3, a straightforward step without the extra step of phase identification.

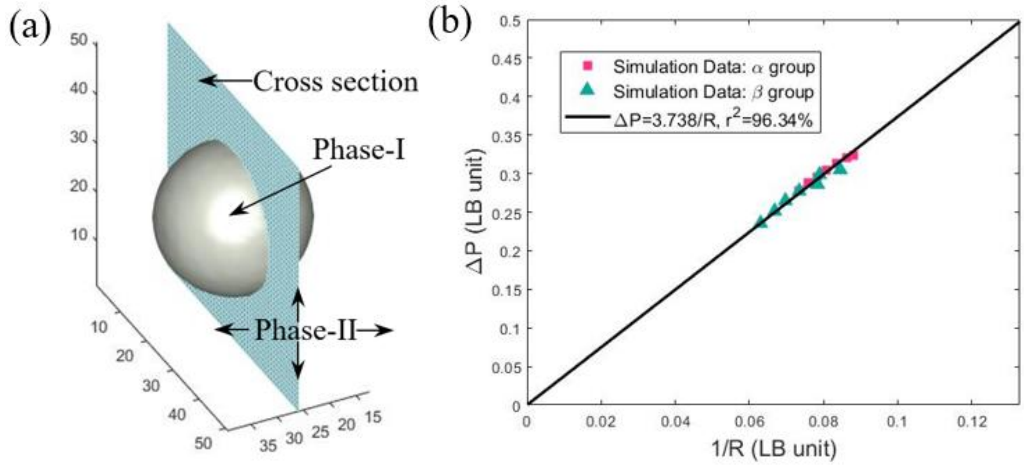

Fig. 2 Validation with Laplace-Young test

The application of the dual matrix computation further enabled the realization of narrowed density difference. Previously (Shan and Chen, 1993), the density inside the bubble was inevitably higher than the external pressure to an order of magnitude of 10, based on which the matrix was identified as high-density fluid and low-density fluid. Consequently, the separation of phases with similar densities became highly challenging since the minor gradual change can hardly support the interface distinguishment. In comparison, the dual-matrix computation in this study performs the collision computation for phase-I and phase-II, respectively. As a result, a solution to obtain separated phases from the beginning (registration) is provided from the program architecture. The 3D phases distribution of phases with relative densities was then tracked throughout the computation. Fig. 3(a) presents the cross-sectional density distribution results of phase-I, and Fig. 3(b) shows the density distribution results of phase-II in the same multi-phase system. Macroscopically, Fig. 3(c) presents the density profile along the measurement area. The stabilized density of phase-I and phase-II was 1.025 and 1.213, respectively. Through adopting the reported coefficients of interaction, the macroscopic densities of water and mercury were realized from a microscopic basis. Fig. 3(d) presents the density gradient profile along the measurement area. The measurement of the bubble radius (R) took the distance between the midpoint of peaks and the whole volume centre. The thickness of the interface region was within 8lu, where lu is the LBM system's unit length (Zhang et al., 2013). Compared with previous single matrix Shan-Chen models, the density difference of the stable phases was reduced from 33% (Parmigiani et al., 2016; Shan and Chen, 1993) to 18%.

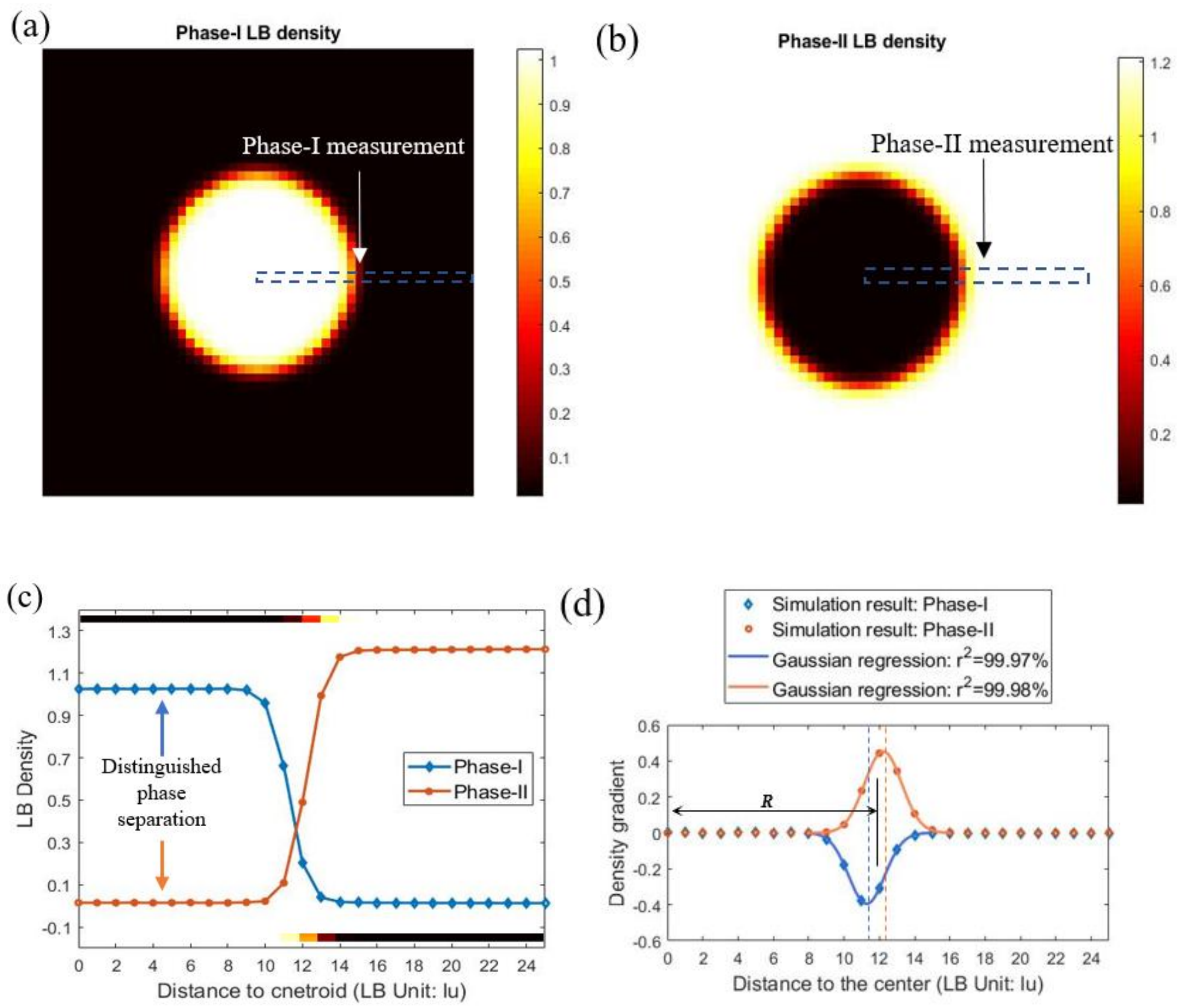

Fig. 3 (a) Cross-sectional of phase-I in the bubble formation simulation. (b) Cross-sectional of phase-I in the bubble formation simulation. (c) LBM Density profile along the measurement area. (d) Density gradient profile along the measurement area.

The surface droplet test was performed with a solid surface, phase-I and phase-II. Fig. 4(a) presents the realized 3D droplet formation of phase-I surrounded by phase-II. Fig. 4(b) illustrates the crossectional result of the visualized data. The contact angle was measured at the intersection of the three phases. The test with phase-I resulted in a contact angle of 38.12°. Fig. 4(c) presents simulation with phase-II surrounded by phase-I, where the non-wetting interaction was realized with 3D density distribution. Fig. 4(d) shows the cross-sectional result of the visualized molecular diffusion, and the resulted contact angle was macroscopically obtained as 142.82°. Consequently, the sum of the two contact angles resulted in 180.94°. Therefore, the wetting (<90°) and non-wetting (>90°) behaviour caused by surface tension was realized. The presented solution for multi-phase separation is essential to obtain the interface between phases with similar density. Hence, securing contact angles becomes consequently possible.

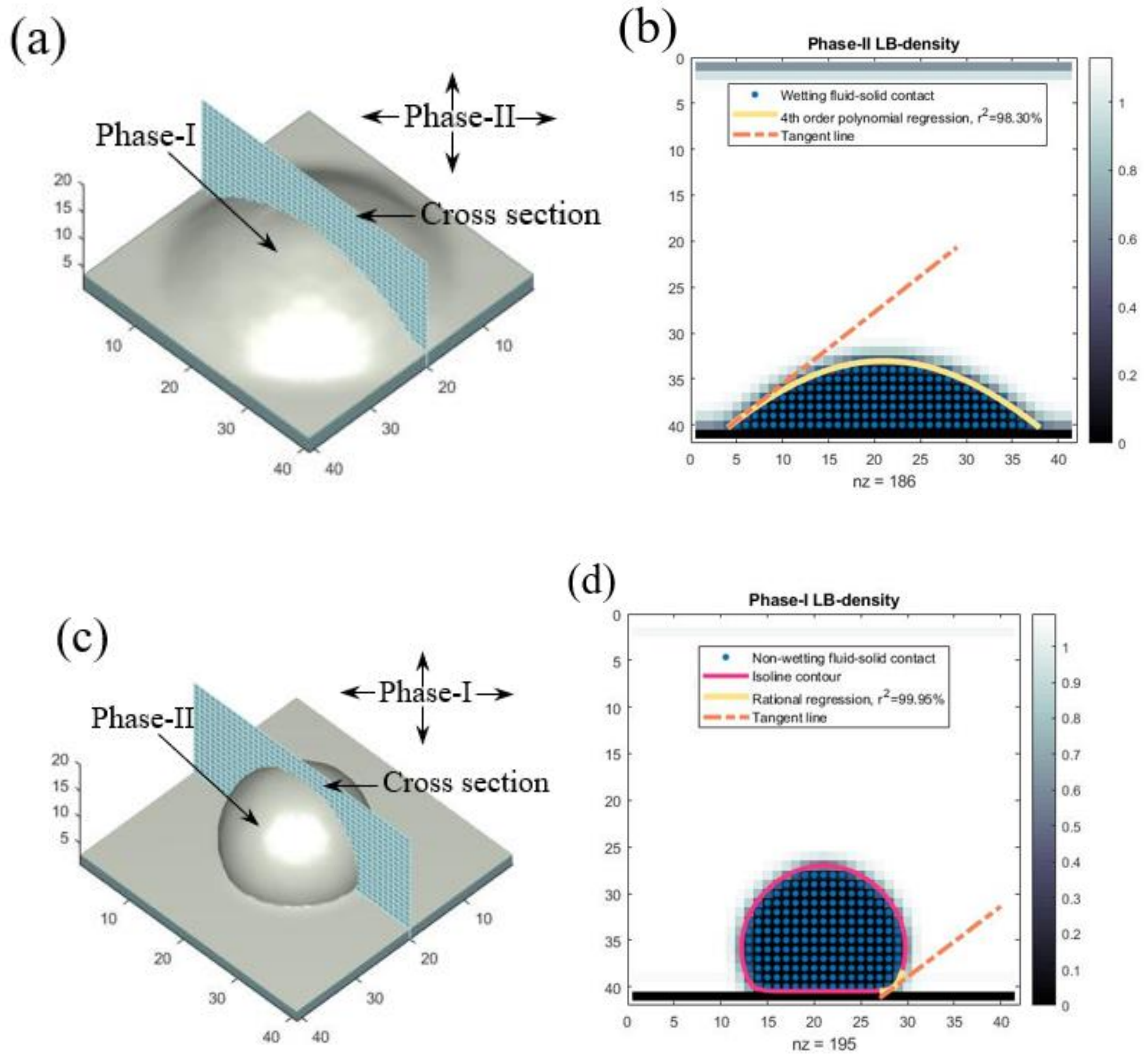

Fig. 4 (a) A wetting surface droplet of phase-I surround by phase-II. (b) The cross-sectional view of (a). (c) A non-wetting surface droplet of phase-II surround by phase-I. (d) The cross-sectional view of (c).

3.2. Application in single-tube scenario

Fig. 5(a). presents the application of the proposed method in a single-tube scenario. The molecular density of phase-II in the top pore initially adopted a uniform distribution with a constant value of

1.5618, which is higher than the target mercury density to initiate intrusion. Fig. 5(b) presents the dynamics process of phase-II from initiation to final stabilization. It was found that the contact angle in the progression stage was higher than in the stabilization stage, which was resulted from the non-equilibrium of the fluid interactions and motion.

Measurement of contact angle resulted in a value of 137.13°, which was 4.14% higher than that of the droplet test. The contact angle difference was caused by the discrete solution to the Boltzmann equation for the arbitrary problem instead of the continuous solution for a particular problem (Gressman and Strain, 2011). The demonstrated application suggests a digital means to control the simulated intrusion behaviour with user-specified densities. The progression of phase-II in the pore-neck is a density increasing process, causing the extension of progression length. The final stabilization indicates a certain progression length within the pore neck under a fixed density difference in the numerical environment.

Consequently, access to the bottom pore of phase-II can be granted when the pore neck is shorter than the progression length. The single-tube intrusion and surface droplet demonstrate the 3D realization of surface tension with the proposed model in fundamental boundaries. The following study presents the performance of the computational framework in more complex scenarios.

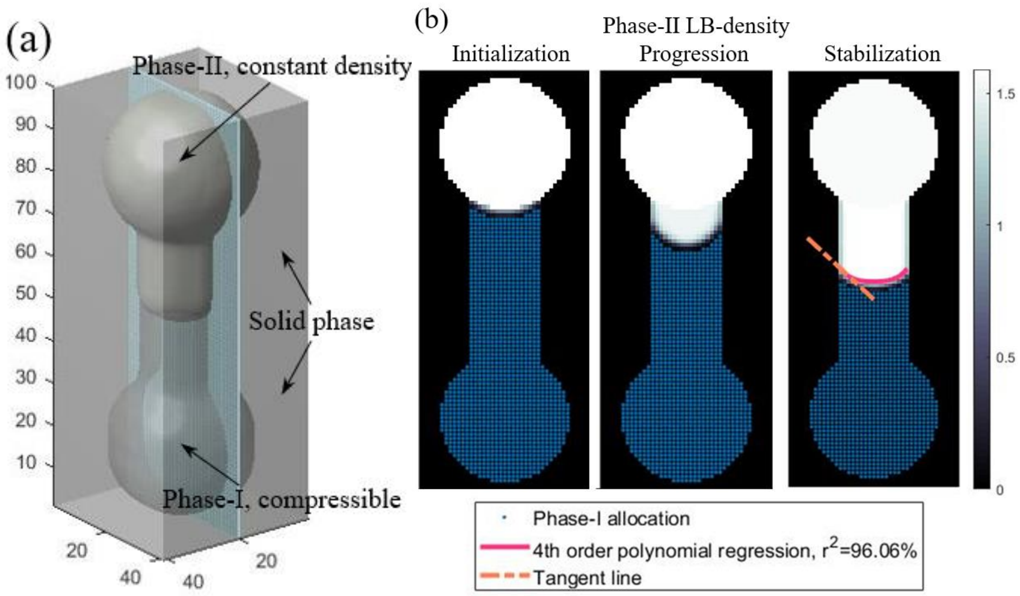

Fig. 5 (a) The virtual device of the pore-neck simulation. (b) Progression process of phase-II.

3.3. Validation with Washburn equation

The multi-tube simulations were performed with a division of isolated tubes, as presented by Fig. 6(a), and a division of connected lines, as shown by Fig. 6(d). Fig. 6(c) demonstrates the virtual device in which the connected tubes simulation was performed. In both divisions, phase-II's initial molecular density in the top volume initially adopted a uniform distribution with a constant value of 1.5618. It was found in the isolated tubes simulation that increased tube radius led to an increment of the progression length. Without 3D distribution, the diffusive Washburn equation previously provided a general description of the relationship between progression depth and tube radius given by Eq.20 (Guancheng and Guancheng, 2018).

$$\mathrm{L} = \sqrt{\frac{\gamma \mathrm{r}_c \mathrm{t} \cos\theta}{2\eta}} \tag{20}$$

Where L is the progression depth, γ is the surface tension, r_c is the tube's radius, t is the progression time, θ is the contact angle, and η is the dynamic viscosity. Under the same Shan-Chen coefficient of interaction and lattice speed of sound, the above parameters were the same controlled variables except for r_c. Eq. 20 indicated that the progression depth L should be in a first-order linear relationship with the square root of the tube radius $\sqrt{\mathrm{r}_c}$. In comparison, Fig. 6(b) presents a successful recovery of the linear relationship from the 3D data independently obtained from the isolated tubes division with a 94.19% coefficient of determination.

The progression depth was governed by both the permeative flow and the diffusive flow in the connected tubes division. Results in Fig. 6(d) shows that the pressure rebalancing caused by the tube interconnection further amended the morphology of the stabilized density distribution. The diameter threshold of the complete intrusion for each tube was previously given by the permeative Washburn equation as given by Eq.21 (Diamond, 2000).

$$\mathrm{d_c} = \frac{-4\gamma\cos\theta}{\mathrm{P}} \tag{21}$$

Where d_c is the diameter of the cylinder being intruded, and P is the pressure. Eq. 21 indicated that a wider tube radius tended to have less difficulty performing intrusion into the opposite volume under the same path length. As a result, intrusion behaviour into porous media naturally processes the function of radius selection. In this study, the radius selection feature was further realized with 3D data of each cross-section, as presented in Fig. 6(d). Results show that the neck radius's increment led to an extended progression length of the digital fluid, and the bottom-up approach has successfully recovered the radius-depth relationship in the classic model. Although Washburn's work has been acknowledged for reflecting the two-phase interaction under his traditional model, it has been an argument that the derivative pore size evaluation method is inappropriate for practical media with increased boundary complexity (Diamond, 2000). The problem raised is that the pore size, pore-neck length and pore morphology cannot be as adequately defined with overly simplified properties, including pore size, porosity and neck length. In the state-of-the-art solution of the multi-phase fluid problem in the heterogeneous boundary, the pore-structure were digitally described with phase information in each 3D coordinate (Shimizu and Tanaka, 2017). After testing the simulated fluid behaviour with limits adopted in previous theories, the feasibility to apply the proposed LBM in the complex boundary is further performed with a porous-medium case in the following section.

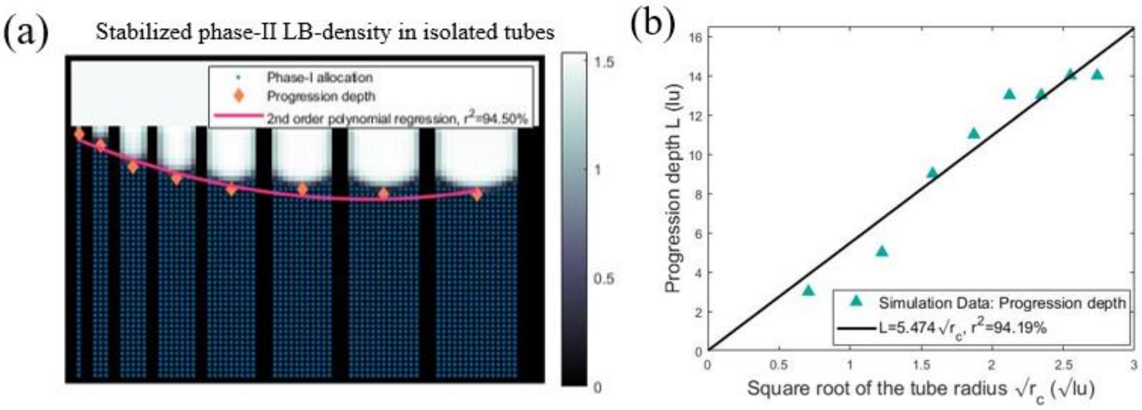

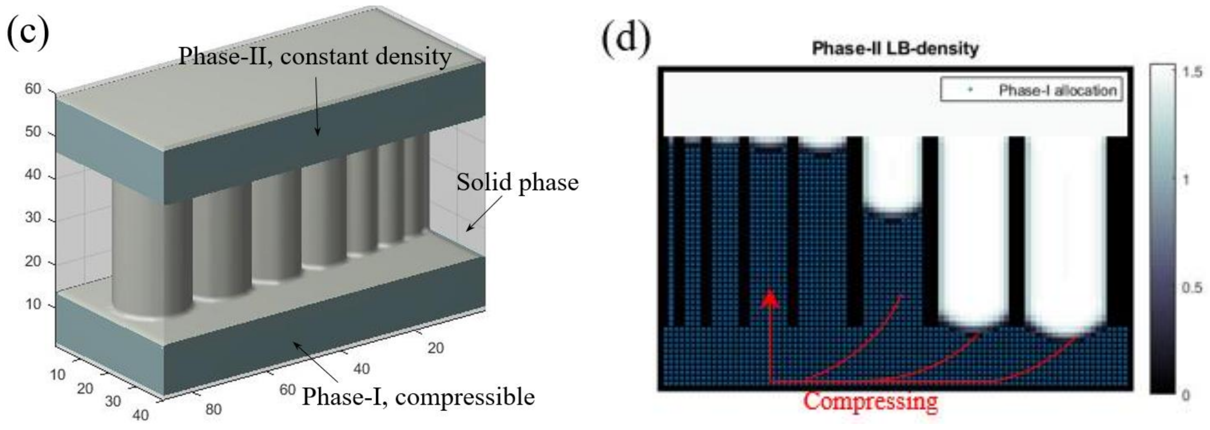

Fig. 6 (a) Simulation with the isolated group. (b) Validation with the Washburn equation Eq. 16. (c) The virtual device of the connected tubes simulation. (c) Simulation with the corresponding group.

3.4. Intrusion into media with increased heterogeneity

Fig. 7 presents the visualized result of phase-II intrusion into a random porous-medium, in which Fig. 7(a) shows the early stage of the intrusion and Fig. 7(b) shows the stabilized phase-II. The cross-sectional results of the simulation are demonstrated by Fig. 7(c) and Fig. 7(d). It was found in the reported realization that phase-II intruded into the porous medium through a path formed by the large pores. Residual phase-I was primarily detected in tiny pores and necks. The decreased intrusion into smaller pores agrees with the practical observation (E. W. Washburn, 1921). Furthermore, results show that the intrusion status into pores with similar sizes was not always identical, which was caused by varying pore-necks. The 3D monitoring of the process suggests that the pores' geometrical influences and pore-necks with irregular shapes can introduce a local variation of phase distribution. Hence, one single parameter of pore size (d_c) is inadequate to reflect the pore space's morphology microscopically. However, the permeative Washburn equation can provide a rough estimation of the pore sizes. Modern computational chemistry has pointed out a solution to the solid-phase representation with a 3D description of each coordinate's information. The work presented in this paper further extend such philosophy towards the fluid phase within.

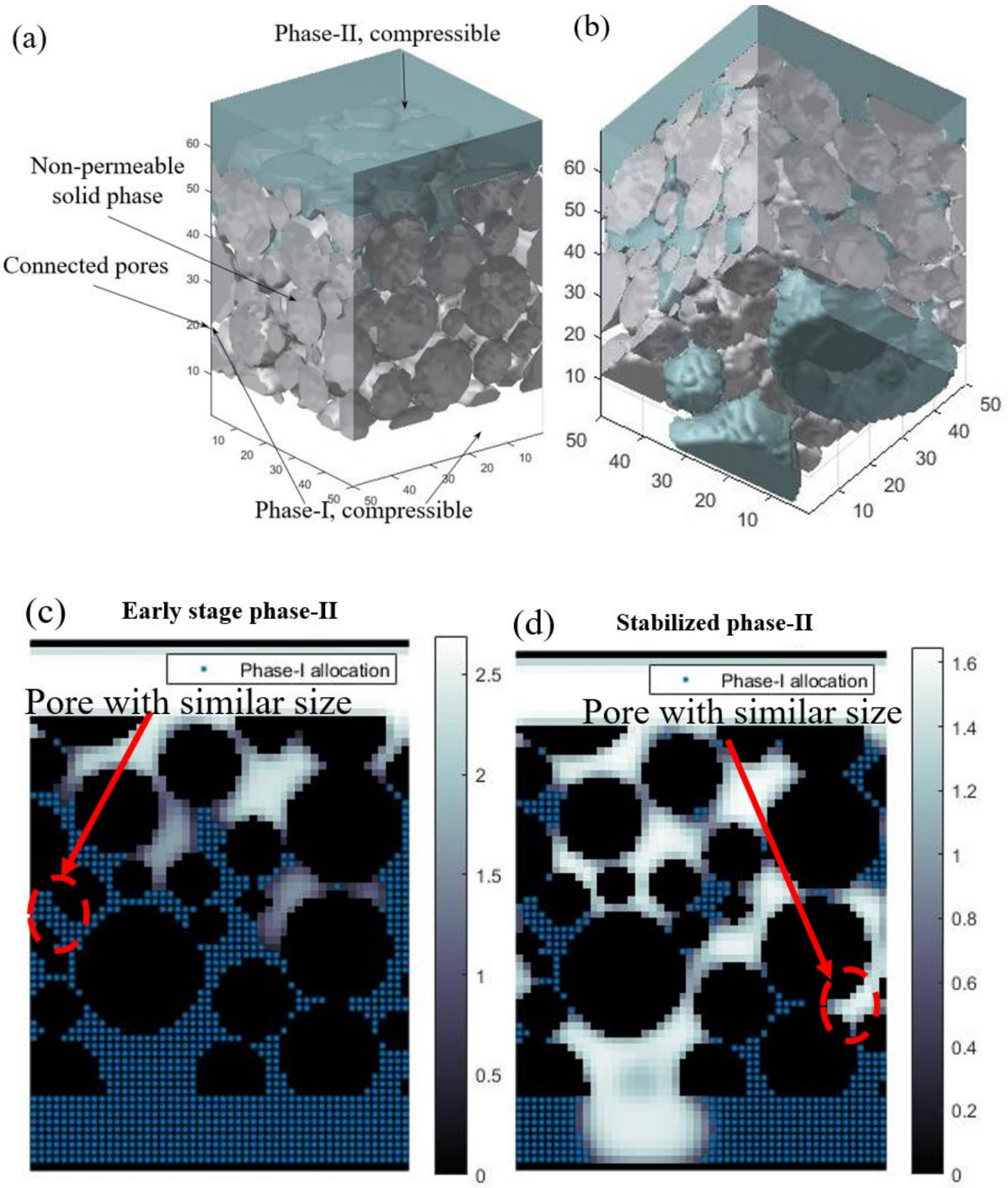

Fig. 7 (a) Visualized results of early-stage phase-II intrusion. (b Visualized results of late-stage phase-II intrusion. (c) 2D cross-sectional view of early-stage phase-II intrusion. (d) 2D cross-sectional view of late-stage phase-II intrusion.

Further investigation was performed with varied phase-II molecular densities upon initialization. Fig. 8(a) presents the 2D cross-sectional results from a uniform density distribution of 4.2, in which the circled area highlight the complete intrusion upon stabilization. In comparison, Fig. 8(b) presents the results from an initial density distribution with 3.2, in which the decreased phase-II pressure resulted in residual phase-I in the circled area. Hence, varied access to irregular-shaped pore driven by different pressure differences was realized with a full map description of molecular density distribution. It is further argued here that fluid-phase intrusion into porous media possesses the third status in addition to complete-intrusion and non-occupation. The squared area in Fig. 8(b) presents a partial intrusion in one of the pore space, whereas the same zone in Fig. 8(a) is of complete-intrusion status. In a non-simplified pore network presented by the adopted porous-medium, the pore morphology's spherical assumption is further invalid since the actual pore is connected with a pore-neck of a non-solid phase. Fig. 8(c) presents the visualized results from applying an intermediate density of 3.8, and the above-discussed pore space shows a noticeable migration of the fluid interface. Fig. 8(d) presents the pore volume's dynamic occupation by phase-II alone with the computational time, whose measurement was three-dimensionally obtained in the zone marked in Fig. 8(c). The results show that the stabilized occupation of phase-II over the volume increased with the raised pressure difference. The in-progress monitoring of the process also describes a rarely discussed behaviour that a retreat of phase-II from the bottom volume occurred before the final stabilization (Fig. 8(d)-ii). In a complex pore network, multiple paths were formed by the solid phase for the fluid intrusion, and the effective length of each path is not necessarily the same. However, the percolation of the global network is simultaneously influenced when a local pore-neck is broken through. Representing the systematic behaviour with final stage outcome and macroscopic properties assembled from the volume is insufficient when a more comprehensive understanding of the system is desired. The clear phase separation provided by the proposed dual-matrix computation enables the above capturing of the fluid interface and the multi-phase 4D molecular density distribution. Through a thorough representation of the molecular map over time and space, computational chemistry predicting detailed information in each coordinate is prepared to investigate beyond the boundary of previous assumptions.

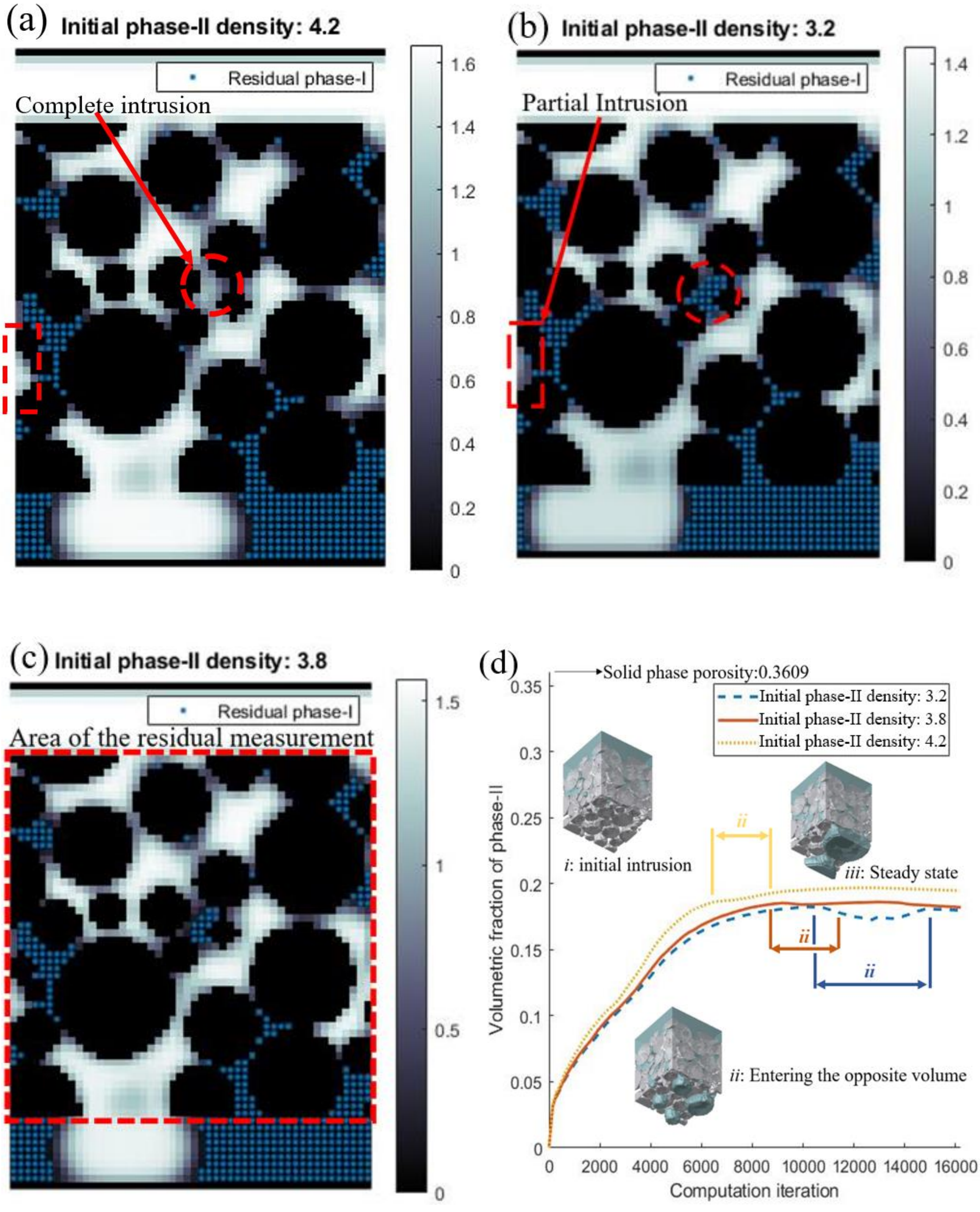

Fig. 8 (a) Local interaction under initial LBM density of 4.2. (b) Local interaction under initial LBM density of 3.2. (c) In-progress monitoring under initial LBM density of 3.8. (d) Macroscopic monitoring of phase-II intrusion.

4. Conclusion

Fluid intrusion into 3D media is a complex process of heterogeneous transport, in which the molecular density distribution is of great significance for chemical engineering. One major challenge to model the process is the different phase separation and interface tracking during the multi-phase evolution within 3D solid boundaries. This work presented a solution to the problem with the proposed dual-matrix computation MRT-LBM initially, enabling in-progress monitoring of separated phases and initialization to stabilization. Application of the kinetics model in the mercury-water system was demonstrated to compare the work with previously theorized observation of capillary dynamics. Results show that narrowed density difference down to 18% was realized with separately tracked 3D fluid distribution in each computational iteration for the first time. Performance of the Laplace-Young test model presented a well-recovered linear relation between pressure difference and the reciprocal of the bubble radius. The droplet test demonstrated a successful integration with the Shan-Chen model to three-dimensionally realize the wetting and non-wetting solid-fluid contact with stabilized contact angles. A further comparison was performed with classic boundaries previously assumed by capillary dynamics after presenting the bottom-up solution's actual performance. Realization in single-tube boundary demonstrates a minor variance of the contact angle result up to only 4.14%. The Washburn equation was recovered under parallel-cylinder limits with a 94.19% coefficient of determination. The sensitivity to cylinder radiused intrusion behaviour was three-dimensionally achieved from the bottom of local surface tension. The spherical assumption in previous capillary dynamics is inadequate to reflect the pore space's morphology in media with increased heterogeneity.

Based on the philosophy of representing heterogeneous media with labelled 3D matrix, this work and its kind extend the systematic description from solid-phase to fluid-phase. Results show that the pressure-dependent access to pores with various sizes was still functional after applying the MRT-LBM in media with increased heterogeneity. However, it was found that phase-II's volumetric occupation was not solely contributed by the difference in access to the pores. The stabilized intrusion processes a status of partial-intrusion in addition to complete-intrusion and non-occupation. The interface migration resulting from varied initial pressure indicates that the local fluid's actual morphology in intruded pores is dynamically modified instead of being constant. The computational realization of intrusion behaviour also presents a time-dependent vision of the simultaneous fluid progression in multiple paths formed by pores. A local breakthrough of the narrow pore-neck in one path resulted in a global retreat of the fluid phase assembled in the other paths. Starting from the current knowledge, the modelling of the 4D behaviour of multi-phase fluid intrusion in realistic media is a challenging task still requiring more specific investigation. The addressed phase-separation and interface-tracking are essential for a comprehensive establishment of the molecular density map's computational description for a broader range of problems in chemical engineering science.

Appendix A. MRT transform matrix

$$
\mathrm{T}=\begin{bmatrix}
1 & 1 & 1 & 1 & 1 & 1 & 1 & 1 & 1 & 1 & 1 & 1 & 1 & 1 & 1 & 1 & 1 & 1 & 1 \\
-30 & -11 & -11 & -11 & -11 & -11 & -11 & 8 & 8 & 8 & 8 & 8 & 8 & 8 & 8 & 8 & 8 & 8 & 8 \\
12 & -4 & -4 & -4 & -4 & -4 & -4 & 1 & 1 & 1 & 1 & 1 & 1 & 1 & 1 & 1 & 1 & 1 & 1 \\
0 & 1 & -1 & 0 & 0 & 0 & 0 & 1 & -1 & 1 & -1 & 1 & -1 & 1 & -1 & 0 & 0 & 0 & 0 \\
0 & -4 & 4 & 0 & 0 & 0 & 0 & 1 & -1 & 1 & -1 & 1 & -1 & 1 & -1 & 0 & 0 & 0 & 0 \\
0 & 0 & 0 & 1 & -1 & 0 & 0 & 1 & 1 & -1 & -1 & 0 & 0 & 0 & 0 & 1 & -1 & 1 & -1 \\
0 & 0 & 0 & -4 & 4 & 0 & 0 & 1 & 1 & -1 & -1 & 0 & 0 & 0 & 0 & 1 & -1 & 1 & -1 \\
0 & 0 & 0 & 0 & 0 & 1 & -1 & 0 & 0 & 0 & 0 & 1 & 1 & -1 & -1 & 1 & 1 & -1 & -1 \\
0 & 0 & 0 & 0 & 0 & -4 & 4 & 0 & 0 & 0 & 0 & 1 & 1 & -1 & -1 & 1 & 1 & -1 & 1 \\
0 & 2 & 2 & -1 & -1 & -1 & 1 & 1 & 1 & 1 & 1 & 1 & 1 & 1 & 1 & -2 & -2 & -2 & -2 \\
0 & -4 & -4 & 2 & 2 & 2 & 2 & 1 & 1 & 1 & 1 & 1 & 1 & 1 & 1 & -2 & -2 & -2 & -2 \\
0 & 0 & 0 & 1 & 1 & -1 & -1 & 1 & 1 & 1 & 1 & -1 & -1 & -1 & -1 & 0 & 0 & 0 & 0 \\
0 & 0 & 0 & -2 & -2 & 2 & 2 & 1 & 1 & 1 & 1 & -1 & -1 & -1 & -1 & 0 & 0 & 0 & 0 \\
0 & 0 & 0 & 0 & 0 & 0 & 0 & 1 & -1 & -1 & 1 & 0 & 0 & 0 & 0 & 0 & 0 & 0 & 0 \\
0 & 0 & 0 & 0 & 0 & 0 & 0 & 0 & 0 & 0 & 0 & 0 & 0 & 0 & 0 & 1 & -1 & -1 & 1 \\
0 & 0 & 0 & 0 & 0 & 0 & 0 & 0 & 0 & 0 & 0 & 1 & -1 & -1 & 1 & 0 & 0 & 0 & 0 \\
0 & 0 & 0 & 0 & 0 & 0 & 0 & 1 & -1 & 1 & -1 & -1 & 1 & -1 & 1 & 0 & 0 & 0 & 0 \\
0 & 0 & 0 & 0 & 0 & 0 & 0 & -1 & -1 & 1 & 1 & 0 & 0 & 0 & 0 & 1 & -1 & 1 & -1 \\
0 & 0 & 0 & 0 & 0 & 0 & 0 & 0 & 0 & 0 & 0 & 1 & 1 & -1 & -1 & -1 & -1 & 1 & 1
\end{bmatrix}
$$

Conflicts of interest

There are no conflicts to declare.

Credit Author Statement

Mingzhi Wang: Conceptualization, Methodology, Software, Validation, Formal analysis, Investigation, Data Curation, Writing - Original Draft, Writing - Review & Editing. **Beimeng Qi:** Investigation, Writing - Review & Editing, Visualization. **Yushi Liu:** Investigation. **Abir Al-Tabbaa:** Supervision. **Wei Wang:** Project administration.

References

Abdoul-Carime, H., Berthias, F., Feketeová, L., Marciante, M., Calvo, F., Forquet, V., Chermette, H., Farizon, B., Farizon, M., Märk, T.D., 2015. Velocity of a molecule evaporated from a water nanodroplet: Maxwell-Boltzmann statistics versus non-ergodic events. Angew. Chemie - Int. Ed. 54, 14685–14689. https://doi.org/10.1002/anie.201505890

Baakeem, S.S., Bawazeer, S.A., Mohamad, A.A., 2020. Comparison and Evaluation of Shan–Chen Model and Most Commonly Used Equations of State in Multiphase Lattice Boltzmann Method. Int. J. Multiph. Flow 103290. https://doi.org/10.1016/j.ijmultiphaseflow.2020.103290

Basser, H., Rudman, M., Daly, E., 2017. SPH modelling of multi-fluid lock-exchange over and within porous media. Adv. Water Resour. 108, 15–28. https://doi.org/10.1016/j.advwatres.2017.07.011

Benzi, R., Biferale, L., Sbragaglia, M., Succi, S., Toschi, F., 2006. Mesoscopic modeling of a two-phase flow in the presence of boundaries: The contact angle. Phys. Rev. E 74, 21509. https://doi.org/10.1103/PhysRevE.74.021509

Bhatnagar, P.L., Gross, E.P., Krook, M., 1954. A model for collision processes in gases. I. Small amplitude processes in charged and neutral one-component systems. Phys. Rev.

Byholm, T., Toivakka, M., Westerholm, J., 2009. Effective packing of 3-dimensional voxel-based arbitrarily shaped particles. Powder Technol. 196, 139–146. https://doi.org/10.1016/j.powtec.2009.07.013

Cantero, M.I., Lee, J.R., Balachandar, S., Garcia, M.H., 2007. On the front velocity of gravity currents. J. Fluid Mech. 586, 1–39. https://doi.org/10.1017/S0022112007005769

Chen, S., Doolen, G.D., 1998. Lattice Boltzmann Method for Fluid Flows. Annu. Rev. Fluid Mech. 30, 329–364. https://doi.org/10.1146/annurev.fluid.30.1.329

Coasne, B., Galarneau, A., Renzo, F. Di, Pellenq, R.J.M., 2009. Intrusion and retraction of fluids in nanopores: Effect of morphological heterogeneity. J. Phys. Chem. C 113, 1953–1962. https://doi.org/10.1021/jp807828a

Coreixas, C., Wissocq, G., Chopard, B., Latt, J., 2020. Impact of collision models on the physical properties and the stability of lattice Boltzmann methods. Philos. Trans. A. Math. Phys. Eng. Sci. 378, 20190397. https://doi.org/10.1098/rsta.2019.0397

D'Humières, D., Ginzburg, I., Krafczyk, M., Lallemand, P., Luo, L.-S.S., 2002. Multiple-relaxation-time lattice Boltzmann models in three dimensions. Philos. Trans. R. Soc. A Math. Phys. Eng. Sci. 360, 437–451. https://doi.org/10.1098/rsta.2001.0955

Dauyeshova, B., Rojas-Solórzano, L.R., Monaco, E., 2018. Numerical simulation of diffusion process in T-shaped micromixer using Shan-Chen Lattice Boltzmann Method. Comput. Fluids 167, 229–240. https://doi.org/10.1016/j.compfluid.2018.03.029

Diamond, S., 2000. Mercury porosimetry. An inappropriate method for the measurement of pore size distributions in cement-based materials. Cem. Concr. Res. 30, 1517–1525. https://doi.org/10.1016/S0008-8846(00)00370-7

Dimitrov, D.I., Milchev, A., Binder, K., 2007. Capillary rise in Nanopores: Molecular dynamics evidence for the Lucas-Washburn equation. Phys. Rev. Lett. 99. https://doi.org/10.1103/PhysRevLett.99.054501

Espinet, A.J., Shoemaker, C.A., 2013. Comparison of optimization algorithms for parameter estimation of multi-phase flow models with application to geological carbon sequestration. Adv. Water Resour. 54, 133–148. https://doi.org/10.1016/j.advwatres.2013.01.003

Gressman, P.T., Strain, R.M., 2011. Sharp anisotropic estimates for the Boltzmann collision operator and its entropy production. Adv. Math. (N. Y). 227, 2349–2384. https://doi.org/10.1016/j.aim.2011.05.005

Guancheng, J., Guancheng, J., 2018. Evaluation Methods and Influencing Factors of Gas Wettability. Gas Wettability Reserv. Rock Surfaces with Porous Media 29–84. https://doi.org/10.1016/B978-0-12-815150-1.00002-X

He, X., Chen, S., Zhang, R., 1999. A Lattice Boltzmann Scheme for Incompressible Multiphase Flow and Its Application in Simulation of Rayleigh-Taylor Instability. J. Comput. Phys. 152, 642–663. https://doi.org/10.1006/jcph.1999.6257

He, X., Luo, L.S., 1997. Theory of the lattice Boltzmann method: From the Boltzmann equation to the lattice Boltzmann equation. Phys. Rev. E - Stat. Physics, Plasmas, Fluids, Relat. Interdiscip. Top. 55, 6811–6820. https://doi.org/10.1103/PhysRevE.56.6811

Hou, D., Yu, J., Wang, P., 2019. Molecular dynamics modeling of the structure, dynamics, energetics and mechanical properties of cement-polymer nanocomposite. Compos. Part B Eng. 162, 433–444. https://doi.org/10.1016/j.compositesb.2018.12.142

Hudgins, R.R., 1981. Inadequacy of the criteria for detecting interphase transport intrusions. Chem. Eng. Sci. 36, 1579–1582. https://doi.org/10.1016/0009-2509(81)85120-2

Huppert, H.E., 1986. The intrusion of fluid mechanics into geology. J. Fluid Mech. 173, 557–594. https://doi.org/10.1017/S0022112086001271

Hyväluoma, J., Raiskinmäki, P., Jäsberg, A., Koponen, A., Kataja, M., Timonen, J., 2004. Evaluation of a lattice-Boltzmann method for mercury intrusion porosimetry simulations. Futur. Gener. Comput. Syst. 20, 1003–1011. https://doi.org/10.1016/j.future.2003.12.013

Khare, V., Dubey, R., Narang, A., 2019. Registration and fusion of CT and MRI images. Int. J. Eng. Adv. Technol. 8, 5017–5021. https://doi.org/10.35940/ijeat.F9113.088619

Kim, T., Kim, G.W.G., Jeong, H., Kim, G.W.G., Jang, S., 2019. Equilibrium structures of water molecules confined within a multiply connected carbon nanotube: A molecular dynamics study.

Phys. Chem. Chem. Phys. 22, 252–257. https://doi.org/10.1039/c9cp05006j

Kuzmin, A., Mohamad, A.A., 2010. Multirange multi-relaxation time Shan-Chen model with extended equilibrium. Comput. Math. with Appl. 59, 2260–2270. https://doi.org/10.1016/j.camwa.2009.08.042

Lacatusu, I., Badea, N., Badea, G., Mihaila, M., Ott, C., Stan, R., Meghea, A., 2019. Advanced bioactive lipid nanocarriers loaded with natural and synthetic anti-inflammatory actives. Chem. Eng. Sci. 200, 113–126. https://doi.org/10.1016/j.ces.2019.01.044

Lane, J.E., Metzger, P.T., Wilkinson, R.A., 2010. A Review of Discrete Element Method (DEM) Particle Shapes and Size Distributions for Lunar Soil. NASA Cent. Aerosp. Inf. 43.

Lee, S.J., Chang, K.S., Kim, S.J., 1998. Surface tension effect in the two-fluids equation system. Int. J. Heat Mass Transf. 41, 2821–2826. https://doi.org/10.1016/S0017-9310(98)00043-X

Limache, A., Idelsohn, S., Rossi, R., Oñate, E., 2007. The violation of objectivity in Laplace formulations of the Navier-Stokes equations. Int. J. Numer. Methods Fluids 54, 639–664. https://doi.org/10.1002/fld.1480

Negahban, S., Kazemi, M., Kalantari, M., Dindoruk, B., Elshahawi, H., 2020. “Digital Fluid Physics”: Prediction of phase equilibria for several mixtures of CO2 with petroleum fluid systems. J. Pet. Sci. Eng. 187. https://doi.org/10.1016/j.petrol.2019.106752

Park, S.H., Weng, J.G., Tien, C.L., 2001. Molecular dynamics study on surface tension of microbubbles. Int. J. Heat Mass Transf. 44, 1849–1856. https://doi.org/10.1016/S0017-9310(00)00244-1

Parmigiani, A., Faroughi, S., Huber, C., Bachmann, O., Su, Y., 2016. Bubble accumulation and its role in the evolution of magma reservoirs in the upper crust. Nature 532, 492–495. https://doi.org/10.1038/nature17401

Perazzo, A., Preziosi, V., Guido, S., 2015. Phase inversion emulsification: Current understanding and applications. Adv. Colloid Interface Sci. 222, 581–599. https://doi.org/10.1016/j.cis.2015.01.001

Pourfattah, F., Toghraie, D., Akbari, O.A., Adhampour, M., Shahsavar, A., 2020. Investigation of mixing process of two different gases in a micromixer: Effect of porous medium and Knudsen number. J. Porous Media 23, 81–99. https://doi.org/10.1615/JPorMedia.2019027028

Premnath, K.N., Abraham, J., 2007. Three-dimensional multi-relaxation time (MRT) lattice-Boltzmann models for multiphase flow. J. Comput. Phys. 224, 539–559. https://doi.org/10.1016/j.jcp.2006.10.023

Qian, Y.H., D’Humières, D., Lallemand, P., 1992. Lattice bgk models for navier-stokes equation. Epl 17, 479–484. https://doi.org/10.1209/0295-5075/17/6/001

Qin, F., Mazloomi Moqaddam, A., Kang, Q., Derome, D., Carmeliet, J., 2018. Entropic multiple-relaxation-time multirange pseudopotential lattice Boltzmann model for two-phase flow. Phys. Fluids 30. https://doi.org/10.1063/1.5016965

Raabe, D., 2004. Overview of the lattice Boltzmann method for nano- and microscale fluid dynamics in materials science and engineering. Model. Simul. Mater. Sci. Eng. 12, R13--R46. https://doi.org/10.1088/0965-0393/12/6/R01

Seiffert, S., 2017. Microfluidics and Macromolecules: Top-Down Analytics and Bottom-Up Engineering of Soft Matter at Small Scales. Macromol. Chem. Phys. 218. https://doi.org/10.1002/macp.201600280

Shan, X., Chen, H., 1994. Simulation of nonideal gases and liquid-gas phase transitions by the lattice Boltzmann equation. Phys. Rev. E. Stat. Phys. Plasmas. Fluids. Relat. Interdiscip. Topics 49, 2941–2948.

Shan, X., Chen, H., 1993. Lattice Boltzmann model for simulating flows with multiple phases and components. Phys. Rev. E 47, 1815–1820. https://doi.org/10.1103/PhysRevE.47.1815

Shan, X., Doolen, G., Chen, H., 1993. Multi-component lattice-Boltzmann model with interparticle interaction. J. Stat. Phys. 81, 379–393. https://doi.org/10.1007/BF02179985

Shimizu, R., Tanaka, H., 2017. Impact of complex topology of porous media on phase separation of binary mixtures. Sci. Adv. 3. https://doi.org/10.1126/sciadv.aap9570

Sun, J., 2018. Permeability of Particle Soils Under Soil Pressure. Transp. Porous Media 123, 257–270. https://doi.org/10.1007/s11242-018-1038-x

Tarek, D.E., Lee, 2018. Uniform regularity for free-boundary Navier-Stokes equations with surface tension. J. Hyperbolic Differ. Equations 15, 37–118. https://doi.org/10.1142/S0219891618500030

Thabet, S., Thabit, T.H., 2018. Computational Fluid Dynamics: Science of the Future. Int. J. Res. Eng. 5, 430–433. https://doi.org/10.21276/ijre.2018.5.6.2

Thomas, L.P., Marino, B.M., Linden, P.F., 2004. Lock-release inertial gravity currents over a thick porous layer. J. Fluid Mech. 299–319. https://doi.org/10.1017/S0022112004007918

Tian, Z., Tian, Y., Ye, H., Jin, X., Jin, N., 2020. VOX model: application of voxel-based packing algorithm on cementitious composites with 3D irregular-shape particles. Mater. Struct. Constr. 53. https://doi.org/10.1617/s11527-020-01512-w

Tiwari, A., Chauhan, S.S., 2019. Effect of varying viscosity on two-fluid model of pulsatile blood flow through porous blood vessels: A comparative study. Microvasc. Res. 123, 99–110. https://doi.org/10.1016/j.mvr.2019.01.003

Ungarish, M., 2005. Intrusive gravity currents in a stratified ambient: Shallow-water theory and numerical results. J. Fluid Mech. 535, 287–323. https://doi.org/10.1017/S0022112005004854

Valentinuzzi, M.E., Kohen, A.J., Zanutto, B.S., 2011. Laplace's law: Its epistemological context. IEEE Pulse 2, 71–76. https://doi.org/10.1109/MPUL.2011.942767

Wang, H., Slamet, N.S., Zhang, G., Chanson, H., 2018. Intrusive measurements of air-water flow properties in highly turbulent supported plunging jets and effects of inflow jet conditions. Chem. Eng. Sci. 177, 245–260. https://doi.org/10.1016/j.ces.2017.11.030

Wang, M., 2017. Numerical modelling of the kinetics and microstructural development of carbonated magnesia-based cements (Doctoral dissertation). University of Cambridge.

Wang, M., Al-Tabbaa, A., Wang, W., 2019. Improving discrete particle packing models for the microstructural formation simulation of Portland cement. Constr. Build. Mater. 229, 116841. https://doi.org/10.1016/j.conbuildmat.2019.116841

Washburn, Edward W., 1921. The dynamics of capillary flow. Phys. Rev. 17, 273–283. https://doi.org/10.1103/PhysRev.17.273

Washburn, E. W., 1921. Note on a Method of Determining the Distribution of Pore Sizes in a Porous Material. Proc. Natl. Acad. Sci. 7, 115–116. https://doi.org/10.1073/pnas.7.4.115

Yoshimoto, Y., Kinefuchi, I., Mima, T., Fukushima, A., Tokumasu, T., Takagi, S., 2013. Bottom-up construction of interaction models of non-Markovian dissipative particle dynamics. Phys. Rev. E - Stat. Nonlinear, Soft Matter Phys. 88. https://doi.org/10.1103/PhysRevE.88.043305

Zhang, J., Tian, F., 2008. A bottom-up approach to non-ideal fluids in the lattice Boltzmann method. Epl 81. https://doi.org/10.1209/0295-5075/81/66005

Zhang, L.Z., 2014. A lattice Boltzmann simulation of mass transport through composite membranes. AIChE J. 60, 3925–3938. https://doi.org/10.1002/aic.14564

Zhang, M., 2013. Multiscale Lattice Boltzman- Finite Element Modelling of Transport Properties in Cement-based Materials. Thechnische University Delft.

Zhang, M., Ye, G., Van Breugel, K., 2013. Microstructure-based modeling of permeability of cementitious materials using multiple-relaxation-time lattice Boltzmann method. Comput. Mater. Sci. 68, 142–151. https://doi.org/10.1016/j.commatsci.2012.09.033

Zhou, C., Ren, F., Wang, Z., Chen, W., Wang, W., 2017. Why permeability to water is anomalously lower than that to many other fluids for cement-based material? Cem. Concr. Res. 100, 373–384. https://doi.org/10.1016/j.cemconres.2017.08.002